CrystEngComm

Accepted Manuscript

ROYAL SOCIETY OF CHEMISTRY

www.rsc.org/crystengcomm

3D Hierarchically Mesoporous Cu-Doped NiO Hierarchical Nanostructures as High-Performance Anodes Materials for Lithium Ion Batteries

Jingyun Ma,[a,b] Longwei Yin*[a], Tairu Ge [a]

[a]Key Laboratory for Liquid-Solid Structural Evolution and Processing of Materials, Ministry of Education, School of Materials Science and Engineering, Shandong University, Jinan 250061, P. R. China

[b]Key Laboratory of Processing and Testing Technology of Glass & Functional Ceramics of Shandong Province, Institute of Materials Science and Engineering, Qilu University of Technology, Jinan 250353, P. R. China

*To whom correspondence should be addressed. Tel.: + 86 531 88396970. Fax: + 86 531 88396970. E-mail: yinlw@sdu.edu.cn

ABSTRACT We report on rational design and synthesis of mesoporous three-dimensional (3D) hierarchical Cu-doped NiO architectures with adjustable chemical component, surface area, and hierarchically porous structure. The effect of Mn doping and calcining temperature on the microstructure, surface area, porous structure of the 3D mesoporous Cu-doped NiO nano-architectures is investigated using SEM, TEM, XPS, XRD, nitrogen adsorption-desorption isotherm techniques. The electrochemical performance of the Cu-doped NiO architectures is studied via cyclic voltammetry (CV), galvanostatic charge-discharge and electrochemical impedance spectroscopy (EIS) techniques. The 3D mesoporous Cu-doped NiO hierarchical architectures display greatly enhanced electrochemical performance of high reversible capacity, high-rate capability, and excellent cycling performance as LIBs anode materials. The improved performance of 3D mesoporous Cu_xNiO anodes can be attributed to the synergetic effects of an optimal level of Cu doping and hierarchically porous feature. The doping of Cu greatly improves charge transport kinetics at the interface between the electrode and electrolyte, and hierarchically porous structure provides larger surface area and allows for effective electrolyte penetration, alleviates the strain induced by volume excursion in cycle processes.

Key words: oxide; porous; microstructure; electrochemical performance; lithium ion battery

1. Introduction

Faced with increasingly depleted non-renewable resources and environmental pollution, the development of the high power and clean energy storage resources is urgently requested.[1] Lithium-ion batteries (LIBs) are deemed to be the dominant high energy and power density sources among sustainable energy supporters for the electronic devices and electric vehicles.[2] However, the requirement for the large scale application in electric vehicles, hybrid electrical vehicles and other power grids, far exceeds the capability of the current LIBs anode materials. Thus, it is greatly fundamental and challenging to develop advanced electrode materials which can meet the growing performance demands.

Transition metal oxides with well-defined morphologies and porous nanostructures have attracted intense research interest as LIBs anode materials due to their primitive high theoretical capacities, porous feature, and high surface area.[3-7] In particular, NiO displays a high theoretical specific capacity of 718 mA h g^{-1}, which is much higher than that of the mostly used graphite anode materials.[8] It is reported that the cycling performance and rate capability of metal oxide are related to the porous structure and surface area.[8] Therefore, many efforts have been made to control the microstructures and surface area of NiO nanostructures, such as nanowires,[9] nanoplates,[10] nanotubes,[11] and hierarchical spheres.[12] However, the low electrical conductivity, poor ion transport kinetics, large volume expansion and contraction occurring in the cycling process, impose great effect on the improvement of electrochemical performance and application of transition metal oxides as LIBs anode materials.[13]

To solve these obstacles, the generally effective route is to design nanostructures and introduce conductive matrix to improve the cycling stability of transition metal oxides by suppressing their volume change and increasing their electrical conductivity.[14,15] Moreover, the hierarchical porosity and hollow structures are involved in newly developed energy storage and conversion system based on transition metal oxides. The hierarchically porous nanostructures assembled from multilevel nanometer scale building blocks display many advantages, such as hierarchically structured pores can provide large surface areas for reaction, interfacial transport, dispersion of active sites at different length scales of pores, and shorten diffusion paths.[16] On the other hand, controlled chemically doping has also been proved to be effective to improve electrical conductivity and further enhance the charge transfer kinetics at the interface between electrode and the electrolyte.[7,18] Recently, Mai et al. reported Co-doped NiO nanoflake arrays show a capacity and rate capability enhancement.[19] The study by Lee's group suggests that Fe-doped Mn_xO_y with hierarchical porosity can deliver a reversible capacity of 620 mA h g^{-1} after 100 cycles at a current density of 200 mA g^{-1}.[20] Despite previous study on the NiO related electrodes, the efficient doping and porous structure tenability of three dimensional mesoporous hierarchical Cu_xNiO architectures as LIBs anode materials are still challenging.

Herein, we present the large-scale synthesis and excellent electrochemical performances of novel 3D hierarchically mesoporous Cu-doped Cu_xNiO architectures as LIBS anode materials with controllable Cu doping contents. The 3D Cu_xNiO nano-architectures with hierarchically porosity were in-situ transformed from Cu doped β-$Ni(OH)_2$ precursors via a calcining process. We realized fine tuning on the hierarchal mesoporous structure and adjustable homogeneously doping of Cu component into lattice of NiO. An optimal chemical doping component of 3%Cu and calcination temperature of 350 °C are determined for the mesoporous 3D hierarchical Cu_xNiO nanostructres as LIBs anode materials with greatly improved electrochemical performance.

2. Experimental

2.1 Preparation of 3D mesoporous hierarchical Cu_xNiO nanostructures

The hierarchical hollow NiO nanostructures were prepared as following steps.[21] Typically, distilled water (76 mL) was used to dissolve nickel (II) chloride hexahydrate ($NiCl_2 \cdot 6H_2O$; 0.975 g, 99%), after adding L-proline ($C_6H_{14}N_2O_2$; 0.345 g, ⩾98%,), the solution was homogenized by magnetic stirrer and stirred for 15 min, 2ml $NH_3 \cdot H_2O$ was dropped into the obtained homogenized solution under the stirring state. After 15 min, the stock solution was transferred into a Teflon-lined stainless steel autoclave and heated at 180 °C for 6.5 h. After cooling to room temperature, the resulted products were washed 3 times with distilled water and ethanol using a centrifuge, respectively, and hen dried at 60 ^{o}C for 12 h. The as-prepared precursor powders were in-situ converted into hollow porous NiO hierarchical nanostructures at a calcinating temperature of 350 ^{o}C for 2 h. Cu_xNiO with different Cu doping contents of 1, 3, 5% were synthesized by controlling the ratio of copper (II) chloride dehydrate ($CuCl_2 \cdot 2H_2O$) and nickel (II) chloride hexahydrate ($NiCl \cdot 6H_2O$), with the appropriate additives of L-proline and aqueous ammonia. To investigate the effects of temperatures on the microstructure evolution of $Cu_{3\%}NiO$, the samples were calcinated at temperature of 350, 450, 550 ^{o}C for 2h, respectively.

2.2 Characterization

The phase and crystalline state of the products were determined by Rigaku D/Max-KA diffractometer equipped with Cu Ka radiation. While the morphology and chemical components were investigated using SU-70 field emission scanning electron microscopy (FE-SEM). The microstructures of the synthesized products were analyzed using transmission electron microscopy (TEM) of JEM-2100 at an acceleration voltage of 200 kV. Nitrogen adsorption-desorption isotherms were determined at 77 K using Gold APP V-Sorb 2800P surface area and porosity analyzer. The surface areas and pore size distribution of the powders were performed using Kelvin equation by means of the Barrett-Joyner-Halenda (BJH) method. X-ray photoelectron spectroscopy (XPS) characterization was carried out in an ESCALAB 250 instru-ment with 150 W Al Ka probe beam.

2.3 Electrochemical measurements

Working electrodes were prepared by mixing 65 wt% active material, 25 wt% acetylene black (Super-P), and 10 wt% polyvinylidene fluoride binder dissolved in N-methyl-2-pyrrolidinone. The mass of active materials for pure NiO, $Cu_{1\%}NiO$, $Cu_{3\%}NiO$, and $Cu_{5\%}NiO$ is about 0.80 mg. The galvanostatic charging and discharging tests were conducted using standard 2032 coin-type cells with copper foil as the current collectors, lithium foil as reference electrodes, a cellgard 2325 as separator and 1.0 M LiPF6 in mixed ethylene carbonate (EC) and diethyl carbonate (DEC) (EC:DEC, 1:1 by volume) as the electrolyte. A cut-off voltage window of 1.0 -3.0 V was used. The 2032 coin-type cells were assembled in an argon-filled glovebox with less than 1 ppm of oxygen and water, galvanostatically cycled on a LAND CT2001A instrument (Wuhan, China) at room temperature. Cyclic voltammetry (CV) measurement was conducted using an electrochemical workstation (PARSTAT 2273) between 1.0-3.0 V at a scan rate of 0.1 mv s^{-1}.

3. Results and discussion

3.1 XRD characterization of $Ni(OH)_2$ and 3D mesoporous hierarchcial Cu_xNiO samples

The crystal structure of the products are identified by X-ray diffraction (XRD) patterns. In Figure 1a, all of the diffraction peaks could be indexed as hexagonal theophrastite structure β-$Ni(OH)_2$ (space group: *P-3ml*, JCPDS: 14-0117). Figure 1b shows the XRD patterns of pure NiO and Cu_xNiO samples with different Cu doping content of 1, 3, 5%, respectively. The diffraction peaks in Fig. 1b are assigned to cubic bunsenite structure NiO (space group: *Fm-3m*, JCPDS: 47-1049). There are no any copper oxide and other impurity phases to be detected. This suggests that β-$Ni(OH)_2$ precursor has completely transformed to cubic NiO during the calcination process. It is supported by the TG-TGA data in the Supporting Information (Figure S1). Figure S1 shows that the decomposition temperature of $Ni(OH)_2$ is about 300 °C, and there is 19.7% total weight loss during the pyrolysis process. Therefore, 350 °C was chosen as the phase transformation temperature to obtain NiO and Cu_xNiO from β-$Ni(OH)_2$ and Cu-doped β-$Ni(OH)_2$ precursors.[12,22] It is indicated from Fig. 1b that the peak intensity of the Cu_xNiO samples gets weaker with the increase of Cu doping content. Figure 1c shows the XRD patterns of the $Cu_{3\%}NiO$ samples annealed at 350, 450 and 550 ^{o}C, respectively. With the calcination temperature increasing, the intensity of the diffraction peaks gets stronger and sharper, indicating that the synthesized products obtained at a higher calcination temperature show higher crystallinity and large grain size. Calculated by the Debye-Scherrer equation, the average size of synthesized samples annealed at temperatures of 350, 450 and 550 ^{o}C, is 10.5, 16.3 and 24.7 nm, respectively.

3.2 SEM and TEM characterization of 3D mesoporous hierarchcial Cu_xNiO samples

The morphology of the precursor Cu-doped $Ni(OH)_2$ could be revealed by field emission scanning electron microscopy (FESEM) and transmission electron microscopy (TEM) (Figure 2). The low magnification FESEM images in Fig. 2a-2b shows that the products are uniformly three-dimensional (3D) hierarchical spherical architectures with an average size of 2 μm. Fig. 2c-2d depicts the high magnification FESEM images of single spherical architecture, showing the 3D spherical architecture is assembled from triangular plates with a thickness of about 40 nm. An open mouth in Fig. 2d suggests that hollow nature for the hierarchical Cu-doped $Ni(OH)_2$ products. The TEM image (Figure 2e) further shows that the Cu-doped $Ni(OH)_2$ products are hollow spherical architectures assembled with triangular plates. The electron diffraction pattern in Fig. 2f suggests a polycrystalline nature for the Cu-doped $Ni(OH)_2$ products. The diffraction rings correspond well to (101), (110), (103), (202) planes of hexagonal Cu-doped $Ni(OH)_2$.

The calcination temperature imposes a key influence on the microstructures of the $Cu_{3\%}NiO$ samples. It is noted that the hierarchical microstructures are completely inherited from the corresponding precursor Cu-doped $Ni(OH)_2$ after thermally calcination treatment. Figure 3a-3b presents low- and high-magnification FESEM images of the $Cu_{3\%}NiO$ products prepared at a calcination temperature of 350 °C for 2 h. It is shown that the as-prepared products display 3D uniformly hierarchical architectures with an diameter of 2 μm, almost maintaining the structural characteristics of the Cu-doped $Ni(OH)_2$ precursor. High magnification FESEM image of a single spherical sample reveals that the 3D hierarchical spherical architectures are composed of triangular plates (Figure S2). With calcination temperature increasing to 450 (Figure 3c-3d) and 550 °C (Figure 3e-3f), the 3D hierarchical microstructures are still completely inherited from the precursor Cu-doped $Ni(OH)_2$ precursors for the obtained hierarchical $Cu_{3\%}NiO$ spherical products. However, although the hierarchical 3D spherical architectures can be steadily maintained, compared with the $Cu_{3\%}NiO$ products obtained at a relatively low calcination temperature of 350 °C, great microstructure evolution takes place for the 450 (Fig. 3c-3d) and 550 °C (Fig. 3e-3f) calcinated samples. Owing to the faster elimination of water molecules from $Ni(OH)_2$ precursor at the relatively higher calcination temperature of 450 and 550 °C, a larger amount of pores could be generated in the calcinated Cu_xNiO

samples. The higher calcination temperature is, the larger pore size and amounts of the pore numbers are generated in the calcinated Cu_xNiO samples. From the high magnification FESEM images in Fig. 3d (450 °C) and Fig. 3f (550 °C), it is shown that with calcination temperature increasing, large amounts of mesopores can be generated in the samples. The detail on the porous structures in the 550 °C can be revealed in Fig. S3. Elemental mapping in Fig. S4 in supporting information shows that Cu, Ni, O are uniformly distributed along the whole products, indicating Cu is homogeneously doped into the lattice of NiO.

Transmission electron microscopy (TEM) was to further describe the porous structures of the obtained Cu_xNiO samples calcinated at different temperatures of 350 and 550 °C, respectively. Figure 4a shows a low magnification TEM image of the $Cu_{3\%}NiO$ sample thermally calcinated at 350°C for 2h. An enlarged TEM image taken from the edge of the 3D hierarchical $Cu_{3\%}NiO$ samples in Fig. 4b clearly suggests the 3D hierarchical $Cu_{3\%}NiO$ sample is composed of two-dimensional (2D) triangular plates. For a 2D triangular Cu_xNiO plate, the magnified TEM image indicates a typical porous structure. The microstructures of $Cu_{3\%}NiO$ sample (Figure 4d-4e) indicate that the 2D plates of $Cu_{3\%}NiO$ are composed of nanocrystals with an average diameter of 10 nm, and mecropores with average size of 8 nm are homogeneously formed within the $Cu_{3\%}NiO$ samples. The four distinct concentric diffraction rings (Figure 4f) could be assigned to (111), (200), (220), (311) planes of cubic $Cu_{3\%}NiO$, which agrees well with the results obtained from the XRD pattern (Figure 1) and TEM images in Fig. 4b-4e.

TEM images in Fig. 5 show the evolution of porous structure of 3D hierarchical $Cu_{3\%}NiO$ samples calcinated at 550 °C for 2 h. A single 3D hierarchical $Cu_{3\%}NiO$ sample in Fig. 5a indicates that porous structures can be obviously revealed in the triangular plates at the edge of the 3D hierarchical $Cu_{3\%}NiO$ sample. Figure 5b-5c give the magnified TEM images of the triangular $Cu_{3\%}NiO$ plates, clearly showing the mesopores of 20-25 nm in the $Cu_{3\%}NiO$ plates. Such larger pores could be derived from the higher thermally treatment at high temperature of 550 °C. Owing to the faster elimination of water molecules from $Ni(OH)_2$ precursor at the relatively higher calcination temperature, mesopores with an average size of 23 nm can be generated in the $Cu_{3\%}NiO$ samples, which is much larger than the average size of 8 nm for the 350 °C calcinated $Cu_{3\%}NiO$ samples. The diffraction rings in the electron diffraction pattern (Fig. 5d) from the center could be assigned to the (111), (200), (220), and (311) planes of cubic $Cu_{3\%}NiO$. The microstructures on the porous structure from TEM result are well in good agreement with the data from the Barrett-Joyner-Halenda (BJH) method for the Brunauer-Emmett-Teller (BET) N_2-adsorption-desorption analysis.

3.3 XPS characterization of 3D mesoporous hierarchcial Cu_xNiO samples

In order to further describe the chemical composition component and chemical bonding state of the Cu_xNiO samples, X-ray photoelectron spectroscopy (XPS) characterization on the $Cu_{3\%}NiO$ sample was carried out (Fig. 6). The survey XPS spectrum for the as-prepared $Cu_{3\%}NiO$ sample in Fig. 6a shows that the product is mainly consisted of Cu, Ni, and O elements. XPS elemental analysis suggests that the atom content of elemental Cu is 2.9%, which is almost in agreement with the theoretical calculated molar ratio value 3%Cu. The presence of C signal may be attributed to adventitious carbon. In the XPS spectra of Ni 2 $P_{3/2}$ (Figure 6b), there are three peaks centered at 853.6, 855.5 and 860.9 eV, respectively. The main peak at 853.6 eV is assigned to Ni^{2+} in the standard Ni-O octahedral bonding configuration in cubic rocksalt $Cu_{3\%}NiO$ samples.[12] The peak centered at 855.5 eV can be ascribed to the Ni 2^+ vacancy-induced Ni^{3+} ion or nickel hydroxides. The broad peak at 860.9 eV can be ascribed to a shakeup process in the NiO structure.[23] Figure 6c depicts the XPS spectrum of Cu 2 $P_{3/2}$, with the main peak centered at 933.3 eV and two shakeup satellite peaks located at 941 and 943.2 eV, respectively. These features correspond to chemical bonding state of Cu ions in the $Cu_{3\%}NiO$ sample, in good consistent with that observed in CuO, [24,25] hence suggesting Cu is incorporated in $Cu_{3\%}NiO$ in the presence of Cu^{2+}. Figure 6d shows the O 1s XPS spectrum of $Cu_{3\%}NiO$ sample, which can be deconvoluted into two peaks. The distinct peak at 529.4 eV corresponds to chemical bonding state of oxygen in NiO,[12,26] The peak at 531.4 eV is ascribed to the shoulder peak of O1s in NiO. The existence of the shoulder peak derives from the surface defect sites within the $Cu_{3\%}NiO$ sample.

3. 4 The nitrogen adsorption-desorption isotherm characterization of 3D mesoporous hierarchcial Cu_xNiO samples

The porous structure of 3D hierarchical mesoporous Cu_xNiO architectures was evaluated by Brunauer-Emmett-Teller (BET) N_2 adsorption-desorption analysis. Figure 7 shows the adsorption-desorption isotherm and the corresponding Barrett-Joyner-Halenda (BJH) pore-size-distribution plots of the 3D hierarchical mesoporous Cu_xNiO architectures. The textural parameters including the BET specific surface area, pore diameter and total pore volume of the $Cu_{3\%}NiO$ thermally treated at 350, 450 and 550 °C, respectively, are summarized in Table 1. Figure 7a exhibits IV type isotherm with a type-H3 loop for samples, showing a disordered mesoporous structure for the 3D hierarchical mesoporous Cu_xNiO samples.[27, 28] With the calcining temperature increasing, the specific surface area of Cu_xNiO sample decreases from 131.7 to 37 and 23.2 $m^2\ g^{-1}$, and the total pore volume displays a similar trend as that of surface area, decreasing from 0.31 to 0.23 and 0.17 $cm^3\ g^{-1}$, respectively. However, the pore diameter displays an inverse trend, increasing from 8.7 nm for 350 °C to 18.9 and 22.4 nm for 450 and 550 °C, respectively (Fig. 7b). The decrease of the surface area and total pore volume, and the increase of the pore diameter of the Cu_xNiO sample, is due to increase of grain size of the Cu_xNiO with calcining temperature increasing, and fast calcination rate at higher temperatures.

Table 1 Structural properties of 3% Cu-doped sample samples annealed at different temperature

Sample	BET surface area /$m^2\ g^{-1}$	Pore diameter /nm	Total pore volume /$cm^3\ g^{-1}$
S350 °C	131.7	8.7	0.31
S450 °C	37.0	18.9	0.23
S550 °C	23.2	22.4	0.17

Figure S5 shows the adsorption-desorption isotherm and corresponding BJH pore size distribution plots of the 3D hierarchical Cu_xNiO architectures with different incorporated Cu contents calcinated at 350 °C. The textural parameters including the BET specific surface area, pore diameter and total pore volume of the Cu_xNiO samples with 0, 1, 3, 5% Cu incorporated contents, are summarized in Table 1. From Fig. S5a, 5c, 5e, 5g, it shows a exhibit a typical type IV isotherm with a H4 hysteresis loop, indicating a disordered mesoporous structure for NiO and Cu_xNiO samples.[22, 27] The BET surface area of Cu_xNiO samples changes gradually with the incorporation content of Cu, from 112 to 119.7, 131.6, 142.7 cm^2 g^{-1} for Cu_xNiO samples (x = 0, 1, 3, 5%). Fig S5b, 5d, 5f, 5h indicate the existence of average pore size of 6.6, 6.8, 3.3, 8.7, 7.6 nm for 0, 1, 3, 5% Cu incorporated Cu_xNiO samples.

3. 5 Mechanism for the formation of 3D mesoporous hierarchcial Cu_xNiO samples

Based on above experimental results, a tentative growth mechanism for the formation of mesoporous 3D hierarchically mesoporous Cu_xNiO nanostructures was proposed (Scheme 1). At first, primary $Ni(OH)_2$ nanocrystalline nuclei are formed in hydrolysis process of $NiCl_2$. As a chelating ligand with a strong coordinating ability, L-proline can coordinate with Ni^{2+} ions to form stable hierarchical structures. At the second step, the grown small $Ni(OH)_2$ nanoparticles are assembled with each other to form nanosheets due to the "oriented attachment" growth process.[29, 30] Subsequently, the bubble of NH_3 acts as soft templates, $Ni(OH)_2$ nanosheets are self-assembled into a sub-micrometer 3D hierarchically hollow architectures. Finally, in the subsequent calcination process, mesoporous 3D hierarchical Cu_xNiO architectures can be formed.[28] The formation of mesoporous structures in the hierarchical Cu_xNiO architectures is due to the faster elimination of water molecules from $Ni(OH)_2$ precursor at the relatively higher calcination temperature. It is shown that the pore size, surface area and pore volume are greatly dependent on the calcination temperature. With calcination temperature increasing, the average size of pores increases, while the surface area and pore volume decrease.[31, 32]

3. 6 Electrochemical characterization of 3D mesoporous hierarchcial Cu_xNiO samples

Figure 8 shows cyclic voltammetric (CV) curves for the first three cycles of pure NiO and Cu_xNiO hierarchical samples at a scan rate of 0.1 mV s^{-1} between the voltage window of 0.01-3.0 V. As revealed from Fig. 8a-b, an important phenomenon is that with the Cu^{2+} doping content increasing, the initial reduction peak at 0.24 V of pure

NiO shifts to higher potential of 0.34, 0.29, and 0.36 V for 1, 3, 5% Cu doped Cu_xNiO samples, and the initial oxidation peaks of the samples almost remain at about 2.3 V. Furthermore, the initial reduction peak intensity of $Cu_{3\%}NiO$ sample is sharper than that of pure NiO sample, and with the Cu doping content increasing, the intensity of the reduction peak of Cu_xNiO samples decreases, indicating an enhanced activity for the electrochemical reaction for the $Cu_{3\%}$doped NiO sample. The electrochemical reaction mechanism of NiO can be described as following: $NiO + 2Li^+ + 2e \rightarrow Li_2O + Ni$. The formation of amorphous Li_2O and metallic Ni is thermodynamically favorable during the discharge process.[33] It is considered that the extraction of Li from Li_2O in the charge process is more difficult, indicating that a certain extent of irreversibility is inevitable. During the subsequent second cycle, different from the first cycle, broad peaks can be clearly observed in the cathodic process for pure NiO (1.0 V), 1%Cu (0.98 V), 3%Cu (0.95 V), and 5%Cu (0.81 V). Also, broad peaks centered at about 2.4, 2.3, 2.45 V and 2.55 V are observed for pure, 1%, 3%, 5% Cu-doped Cu_xNiO samples during the anodic polarization process, corresponding to the oxidation of Ni^0 to Ni^{2+}.

In the third cycle, the cathodic and anodic plots are similar to the second cycle, almost overlapping each other respectively. Compared to pure NiO and 1%, 5% Cu-doped Cu_xNiO samples, the intensity of cathodic peaks for $Cu_{3\%}NiO$ electrodes at near 0.3 V is much stronger, and the integral area of anodic peak locating at near 1.0 V is larger than any other Cu_xNiO samples. This is mainly attributed to the improved electronic conductivity of $Cu_{3\%}NiO$ electrode than any other samples, which facilitates the faster charge transfer kinetics for redox processes of solvent molecules in electrolyte related to the formation of solid electrolyte interphase (SEI) layer.[19, 34,35, 36]

Figure 9a-d shows the 1st, 2nd, 3rd, 4th and 5th cycle discharge/charge curves of pure NiO and Cu_xNiO with different Cu doping contents (x = 1%, 3%, 5%) at a current density of 100 mA g^{-1} between 0.01 V and 3.0 V at room temperature. The pure NiO and Cu_xNiO samples show initial discharge capacity of 1182, 1406, 1299 and 1168 mA h g^{-1}, and initial charge capacity of 847, 1019, 961, 839 mA h g^{-1}, respectively, displaying the initial coulombic efficiency of 71.7%, 72.5%, 74% and 71.9%, respectively. The capacity loss in the first cycle could be attributed to electrolyte decomposition and the formation of a SEI layer. At the 5th cycle, it is shown that the $Cu_{3\%}NiO$ electrode shows the best electrochemical performance, displaying the reversible charge capacity of 781, 950, 984 and 826 mA h g^{-1} (for 0, 1, 3, 5% Cu content), corresponding to coulombic efficiency of 96.9, 97.1, 98.5, 98.1%, respectively. With the increase of Cu doping content, the reversible capacity of the Cu_xNiO samples first rapidly increases and then decreases as Cu doping molar percentage is up to 3%. Moreover, the two distinct voltage plateau can be observed clearly at around 0.5 V and 2.2 V corresponding to the initial cathodic and anodic peaks during the CV process described in Fig. 8.

The chemical composition component and the microstructures such as grain size, crystallinity, porous structure, surface area and pore volume should impose key effects on the electrochemical performance of the mesoporous 3D hierarchical Cu_xNiO architectures. For the effect of Cu incorporation content on the cycling performance and stability, at a galvanostatic charge/discharge current of 100 mA g^{-1} between 0.01 and 3.0 V, it can be comparatively illustrated in Fig. 10a. Among the Cu_xNiO samples with different Cu incorporated contents, the $Cu_{3\%}NiO$ sample delivers the highest specific capacity of 550 mA h g^{-1} after 100 cycles with a coulombic efficiency of 97.1%. By a comparison, the pure NiO and the $Cu_{1\%}NiO$, $Cu_{5\%}NiO$ electrode could only display reversible charge capacity of 184 and 376, 272 mA h g^{-1} after 100 cycles, respectively. It is clearly shown that the reversible capacity of $Cu_{3\%}NiO$ after 100 cycles at a current density of 100 mA h g^{-1} is 2.98 and 2.0 times higher than that of the pure NiO and $Cu_{5\%}NiO$ electrodes. Hence, the electrochemical performance of mesoprous hierarchical Cu-doped NiO is improved by Cu doping into lattice of NiO. However, the content of Cu-doping needs to be carefully controlled, as an excess of Cu doping may lower the discharge capacity in extended cycling.[37] As the Cu doping content increases to 3%, the $Cu_{3\%}NiO$ sample displays the highest specific capacity of 550 mA h g^{-1} after 100 cycles. After that, the increase in the Cu doping content may lower the performance. In the case of $Cu_{5\%}NiO$ sample, the mesopores were constricted by a more compact packing of the primary nanocrystallites, decreasing the accessibility of electrolyte to electroactive electrode as a result, and thus a lackluster cycling performance was obtained.[20] It indicates that the importance of a moderate level for Cu doping to balance its effects on interfacial charge transfer and the structural integrity of the mesopores. The departure from a proper balance would inevitably incur a compensatory outcome.[20] Here, 3% mole ratio of doping for NiO is the closest optimized level spot. It is distinctly indicated that $Cu_{3\%}NiO$ sample shows a much more excellent cycle specific capacity than that of previously reported NiO-based materials, as shown in Table 2.

Table 2 Cycling and rate performance of the $Cu_{3\%}NiO$ compared with those of other NiO materials

Samples	Cycle number	Reversible capacities (mA h g^{-1})	Reference
Grapheme/NiO	40	716 (300 mA g^{-1})	38
3D flower like NiO	40	713 (100 mA g^{-1})	39
CuO-NiO nanocomposites	50	562.5 (80 mA g^{-1})	40
CuNiO/CNT(carbon nanotube)	50	686 (100 mA g^{-1})	41
NiO nanosphere	60	518 (100 mA g^{-1})	42
$Cu_{3\%}NiO$	100	550 (100 mA g^{-1})	This work

Figure 10b comparatively shows the rate capability of the Cu_xNiO calcinated at 350°C, with Cu incorporation content of 0, 1, 3, 5%. After 10 cycles at a current density of 100 mA g^{-1}, the Cu_xNiO samples show the reversible capacity of 713, 828, 977, and 921 mA h g^{-1} for 0, 1, 3, 5% Cu-doped Cu_xNiO samples. At a current density of 200 mA g^{-1}, the 20th reversible capacity is 445, 601, 743, and 636 mA h g^{-1} for 0, 1, 3, 5% Cu-doped Cu_xNiO samples, respectively. Even after 40 cycles at a current density of 1600 mA g^{-1}, the reversible capacity of the electrodes can retain 106, 251, 390, 158 mA h g^{-1} for 0, 1, 3, 5% Cu-doped Cu_xNiO samples. As the current density returns to 100 mA g^{-1}, the reversible specific capacity can remain at a value of 601, 694, 840, 665 mA h g^{-1} for 0, 1, 3, 5% Cu-doped Cu_xNiO samples, respectively. As is revealed, $Cu_{3\%}NiO$ sample presents significantly improved rate capability in comparison with the other electrodes. Even at the high current density of 1600 mA g^{-1}, the reversible capacity still retains at value of 390 mA h g^{-1}, which is 3.6 times higher than that of pure NiO electrode. When the current density returns to 100 mA g^{-1}, the reversible capacity can be recovered to 840 mA h g^{-1}. The improved electrochemical performance of the 3D mesoporous hierarchical mesoporous Cu_xNiO electrode can be attributed to their unique interconnected porous hollow microstructures, high surface area. The improved kinetic of porous structure and mesoporous NiO crystals are tolerant of various charge and discharge currents, which is preferred for high power applications.[43,44] More importantly, the effectively doping of Cu not only renders fast kinetics to facilitate electron transportation and Li^+ ion insertion/deinsertion but also relieves the stress caused by volume changes during the charge/discharge cycles.[45-47]

The above microstructure analysis shows that temperature imposes great effect on the surface area, pore size and pore volume of the calcinated Cu_xNiO samples. Figure 11 depicts the influence of annealing temperature on the cycling performance of $Cu_{3\%}NiO$ sample. Clearly, as increasing the calcination temperature from 350 to 550 °C, the reversible capacity retention of $Cu_{3\%}NiO$ sample significantly decreases. At the 20th cycle, the reversible capacity is 967, 613, 670 mA h g^{-1} for 350, 450 and 550 °C calcinated $Cu_{3\%}NiO$ samples. However, during the 20th to 80th cycle, the reversible capacity of 550 °C sample decreases greatly compared to that of 350 and 450 °C calcinationed $Cu_{3\%}NiO$ sample, showing a reversible capacity of 323 mA h g^{-1} at a current density of 100 mA h g^{-1}, much lower than that of 562, 386 mA h g^{-1} for 350 °C and 450 °C calcinated $Cu_{3\%}NiO$ samples, respectively. At the 100th cycle, the 350 °C calcinated $Cu_{3\%}NiO$ sample still displays a reversible capacity of 550 mA h g^{-1} at a current density of 100 mA g^{-1}, which is much higher than that of 381 and 282 mA h g^{-1} for 450 and 550 °C calcinated $Cu_{3\%}NiO$ samples. Figure S6 shows the performance of rate capability for the $Cu_{3\%}NiO$ samples calcinated at 350 and 550 °C, suggesting the superior rate capability for 350 °C calcinated $Cu_{3\%}NiO$ samples than that calcinated at 550 °C.

The improved performance of hierarchically mesoporous Cu_xNiO architectures as LIBs anode materials could be attributed to the synergetic effects of an optimal level of Cu doping, hierarchically porous feature and hollow structure that concurrently takes place in the Li ion charge-discharge process. Firstly, the doping of Cu into lattice of NiO can greatly improve the charge transport kinetics taking place at the interface between the electrode and electrolyte (Figure S7), the optimized Cu doping of 3% $Cu_{3\%}NiO$ electrode exhibits lower impedance than that of pure and other Cu_xNiO samples, resulting in performance enhancement of Li ion storage.[20] Secondly, hierarchically porous structure could provides larger surface area and allow for effective electrolyte penetration, reduce mass transfer limitations, and alleviates the strain induced by volume excursion in discharge and charge processes.[15, 48, 49] Thirdly, the triangular nanoplate building blocks and the hollow interior can provide efficient transport of Li^+ ions because of the short diffusion length and the highly porous structure.[50, 51]

4. Conclusions

We report on the large-scale synthesis and excellent electrochemical performances of novel 3D hierarchically mesoporous Cu-doped Cu_xNiO architectures as LIB_S anode materials with controllable Cu doping contents. The 3D Cu_xNiO nano-architectures with hierarchical porosity were in-situ transformed from Cu doped β-$Ni(OH)_2$ precursors via a calcining process. We realized fine tuning on the hierarchically mesoporous structure via controlling the calcination temperature, also homogeneously adjustable doping of Cu component into lattice of NiO. It is shown that an optimal chemical doping component of 3%Cu and calcination temperature of 350 ^oC are determined for the 3D mesoporous hierarchical Cu_xNiO nanostructres as LIBs anode materials with excellent Li ion storage performance. The $Cu_{3\%}NiO$ sample calcinated at 350 ^oC delivers the highest specific capacity of 550 mA h g^{-1} after 100 cycles with a coulombic efficiency of 97.1%, which is 2.98 and 2.0 times higher than the reversible capacity of the pure NiO and $Cu_{5\%}NiO$ electrodes. The novel 3D mesoporous Cu_xNiO hierarchical architectures as LIBs anode materials also display greatly enhanced high-rate capability performance of Li ion electrochemical storage, and excellent cycling performance. The great improvement of the electrochemical performance can be attributed to the synergetic effects of Cu doping with an optimal level, hierarchically porous feature and hollow structure of the Cu_xNiO samples.

Acknowledgments

We acknowledge support from the National Natural Science Funds for Distinguished Young Scholars (No: 51025211), National Basic Research Program (No: 2013CB934303), National Nature Science Foundation of

China (No: 51272137), the Tai Shan Scholar Foundation of Shandong Province.

References

1. C. Liu, F. Li, L.P. Ma, H.M. Cheng, *Adv. Mater*., 2010, 22, E28.

2. F.Cheng, J. Liang, Z. Tao, J. Chen, *Adv. Mater*., 2011, 23, 1695.

3. K.A. Kwon, H.S. Lim, Y.K. Sun, K.D. Suh, *J. Phys. Chem. C*, 2014, 118, 2897.

4. M.W. Xu, Y.B. Niu, S.J. Bao, C.M. Li, *J. Mater. Chem. A*, 2014, 2, 3749.

5. N. Du, H. Zhang, B.D. Chen, J.B. Wu, X.Y. Ma, Z.H. Liu, Y.Q. Zhang, D.R. Yang, X.H. Huang, J.P. Tu, *Adv. Mater*., 2007,19, 4505.

6. J. Liu, Y. Zhou, C. Liu, J. Wang, Y. Pan, D. Xue, *CrystEngComm*., 2012, 14, 2669.

7. F. Miao, Q. Li, B. Tao, P.K. Chu, *J. Alloys Compd*., 2014, 594, 65.

8. D. Su, M. Ford, G. Wang, *Scientific reports*, 2012, 2, 924.

9. D. Su, H.S. Kim, W.S. Kim, G. Wang, *Chem. Eur. J*., 2012, 18, 8224.

10. A. Caballero, L. Hernán, J. Morales, Z. González, A.J. Sánchez-Herencia, B. Ferrari, *Energy Fuels*, 2013, 27, 5545.

11. V. Bini, M.V. Reddy, Z. Yanwu, C.S. Lit, T.C. Hoong, G.V.S. Rao, B.V.R. Chowdari, A.T. Wee, C.T. Lim, C.H. Sow, *Chem. Mater*., 2008, 20, 3360.

12. B. Zhao, X.K. Ke, J.H. Bao, C.L. Wang, L. Dong, Y.W. Chen, H.L. Chen, *J. Phys. Chem. C*, 2009, 113,14440.

13. J. Jiang, Y. Li, J. Liu, X. Huang, C. Yuan, X.W. Lou, *Adv. Mater.*, 2012, 24, 5166.

14. D. Liu, G. Cao, *Energy Environ. Sci*., 2010, 3, 1218.

15. Y. Xia, W. Zhang, Z. Xiao, H. Huang, H. Zeng, X. Chen, F. Chen, Y. Gan, X. Tao, *J. Mater. Chem*., 2012, 22, 9209.

16. Y. Li, Z.Y. Fu, B.L. Su, *Adv. Funct. Mater.*, 2012, 22, 4634.

17. Y. Ma, B. Ding, G. Ji, J.Y. Lee, *ACS Nano*, 2013, 7, 10870.

18. Q. Wang, Y. Huang, J. Miao, Y. Zhao, Y. Wang, *Electrochimica Acta*, 2013, 93, 120.

19. Y.J. Mai, J.P. Tu, X.H. Xia, C.D. Gu, X.L. Wang, *J. Power Sources*, 2011, 196, 6388.

20. Y. Ma, C. Fang, B. Ding, G. Ji, J.Y. Lee, *Adv. Mater*., 2013, 25, 4646.

21. Y. Yan, H.B. Li, J.F. Li, J. Pan, Y.T. Qian, Chinese J. *Inorg. Chem*., 2010, 26, 1141.

22. S.I. Kim, J.S. Lee, H.J. Ahn, H.K. Song, J.H. Jang, ACS Appl. *Mater. Interfaces*, 2013, 5, 1596.

23. J.R. Manders, S.W. Tsang, M.J. Hartel, T.H. Lai, S. Chen, C.M. Amb, J.R. Reynolds, *Adv. Funct. Mater*., 2013, 23, 2993.

24. C.K. Wu, M. Yin, S. O'Brien, J.T. Koberstein, *Chem. Mater.*, 2006, 18, 6054.

25. L. Martin, H. Martinez, D. Poinot, B. Pecquenard, F. Le Cras, *J. Phys. Chem. C*, 2013,117, 4421.

26. G. Zhou, D.W. Wang, L.C. Yin, N. Li, F. Li, H.M. Cheng, *ACS Nano*, 2012, 6, 3214.

27. R. Wang, C. Xu, J. Sun, L. Gao, H. Yao, ACS Appl. *Mater. Interfaces*, 2014, 6, 3427.

28. Y. Liu, Y. Jiao, Z. Zhang, F. Qu, A. Umar, X. Wu, *ACS Appl. Mater. Interfaces*, 6, 2174.

29. R.L. Penn, *Science*, 1998, 281, 969.

30. J.F. Banfield, *Science*, 2000, 289, 751.

31. J.C. Yu, A. Xu, L. Zhang, R. Song, L. Wu, *J. Phys. Chem. B*, 2004, 108, 64.

32. Q. Li, Y. Chen, T. Yang, D. Lei, G. Zhang, L. Mei, L. Chen, Q. Li, T. Wang, *Electrochim. Acta*, 2013, 90, 80.

33. S.H. Choi, Y.C. Kang, *ACS Appl. Mater. Interfaces*, 2014, 6, 2312.

34. M.C. Yang, B. Xu, J.H. Cheng, C.J. Pan, B.J. Hwang, Y.S. Meng, *Chem. Mater*., 2011, 23, 2832.

35. M. Sasidharan, N. Gunawardhana, C. Senthil, M. Yoshio, *J. Mater. Chem A*, 2014, 2, 7337.

36. Z. Ali, S.N. Cha, J.I. Sohn, I. Shakir, C. Yan, J.M. Kim, D.J. Kang, *J. Mater. Chem*, 2012, 22, 17625.

37. C. Chen, Y. Huang, C. An, H. Zhang, Y. Wang, L. Jiao and H. Yuan. *ChemSusChem*, **2015**, 8, 114-122.

38. S-G. Hwang,G-OK. Kim, S-R. Yun, K-S. Ryu. *Electrochimica Acta*, 2012, 78, 406.

39. Q. Li, Y. Chen, T. Yang, D. Lei, G. Zhang, L. Mei, L. Chen, Q. Li, T. Wang. *Electrochimica Acta*, 2013, 90,

80.

40. H. Chen, C-L. Li, N. Li, K-X. Xiang, Z-L. Hu. *Micro & Nano Letters*, 2013, 8, 544.

41. S. M. Abbas, S. T. Hussain, S. Ali, N. Ahmad, N. Ali, S. Abbas, Z. Ali. *Journal of Solid State Chemistry*. 2013, 202, 43.

42. G. Zhang, Y. Chen, B. Qu, L. Hu, L. Mei, D. Lei, Q. Li, L. Chen, Q. Li, T. Wang. *Electrochimica Acta*, 2012, 80, 140.

43. Z. Bai, X. Zhang, Y. Zhang, C. Guo and B. Tang. *J. Mater. Chem. A*, 2014, 2, 16755.

44. Z. bai, Z. Ju, C. Guo, Y. Qian, B. Tang and S. Xiong. *Nanoscale*, 2014, 6, 3268.

45. J.G. Kim, M.S. Park, S.M. Hwang, Y.U. Heo, T. Liao, Z. Sun, J.H. Park, K.J. Kim, G. Jeong, Y.J. Kim, J.H. Kim, S.X. Dou, *ChemSusChem*., 2014, 7, 1451.

46. X.L. Wang, W.Q. Han, H. Chen, J. Bai, T.A. Tyson, X.Q. Yu, X.J. Wang, X.Q. Yang, *J. Am. Chem. Soc*., 2011, 133, 20692.

47. Z.Y. Wang, L. Zhou, X.W. Low, *Adv. Mater*., 2012, 24, 1903.

48. C. Zhang, Z. Chen, Z. Guo, X.W. Lou, *Energy Environ. Sci*., 2013, 6, 974.

49. A. Vu, Y. Qian, A. Stein, *Adv. Energy Mater*., 2012, 2, 1056.

50. B. Wang, H.B. Wu, L. Zhang, X.W. Lou, *Angew. Chem. Int. Ed*., 2013, 52, 4165.

51. L. Yu, H.B. Wu, X.W. Lou, *Adv. Mater*., 2013, 25, 2296.

Figure captions

Figure 1. X-ray diffraction (XRD) patterns for (a) $Ni(OH)_2$ precursor, (b) pure NiO and Cu_xNiO with 1, 3, 5% incorporated Cu contents. (c) Comparison of XRD patterns for $Cu_{3\%}NiO$ calcinated at 350, 450, 550°C, respectively.

Figure 2 (a-d) Low- and high-magnification FESEM images of 3D hierarchical Cu-doped $Ni(OH)_2$ products spherical architectures. (e) Low magnification TEM image of Cu-doped $Ni(OH)_2$. (f) Electron diffraction pattern suggests a polycrystalline nature for the Cu-doped $Ni(OH)_2$ products. The diffraction rings correspond well to (101), (110), (103), (202) planes of hexagonal Cu-doped $Ni(OH)_2$.

Figure 3 (a-b), (c-d), (e-f) Low- and high-magnification FESEM images of the $Cu_{3\%}NiO$ products prepared at a calcination temperature of 350, 450, 550°C for 2 h, respectively.

Figure 4 (a) Low magnification TEM image of $Cu_{3\%}NiO$ sample thermally calcinated at 350°C. (b) An enlarged TEM image taken from the edge of the 3D hierarchical $Cu_{3\%}NiO$ samples in Fig. 4b clearly suggests the 3D hierarchical $Cu_{3\%}NiO$ sample is composed of two-dimensional (2D) triangular plates. (c) A magnified TEM image indicates a typical porous structure for $Cu_{3\%}NiO$ sample. (d-e) High magnification TEM images indicate and mecropores with average size of 8 nm are homogeneously formed within the $Cu_{3\%}NiO$ samples, and $Cu_{3\%}NiO$ plates are composed of nanocrystals with an average diameter of 10 nm. (f) Electron diffraction concentric diffraction rings could be assigned to (111), (200), (220), (311) planes of cubic $Cu_{3\%}NiO$.

Figure 5 (a) Low magnification TEM image of $Cu_{3\%}NiO$ sample thermally calcinated at 550°C. (b-c) Magnified TEM images of the triangular $Cu_{3\%}NiO$ plates, clearly showing the porous structure with an average size of 20-25 nm for the pores in the $Cu_{3\%}NiO$ samples. Such larger pores could be owing to the faster elimination of water molecules from $Ni(OH)_2$ precursor at the relatively higher calcination temperature. (d) The diffraction rings could be assigned to the (111), (200), (220), and (311) planes of cubic $Cu_{3\%}NiO$.

Figure 6 (a) Survey XPS spectrum for the as-prepared $Cu_{3\%}NiO$ sample. (b) XPS spectra of Ni 2 $P_{3/2}$. (c) XPS spectrum of Cu 2 $P_{3/2}$. (d) O 1s XPS spectrum of $Cu_{3\%}NiO$ sample.

Figure 7 Porous structure analysis of $Cu_{3\%}NiO$ samples calcinated at 350, 450, 550°C, respectively. (a) Nitrogen adsorption/desorption isotherm and (b) pore size distribution.

Scheme 1 Schematic illustration for the possible growth of as-synthesized hierarchical hollow mesoporous Cu_xNiO nanostructures.

Figure 8 (a, b) CV curves for three cycles at a scan rate of 0.1 mV s^{-1} in the voltage range of 3.00-0.01 V of the pure NiO, Cu_xNiO samples calcinated at 350°C with different Cu incorporated contents of 1, 3, 5%, respectively.

Figure 9. Discharge-charge profiles of electrode at a current density of 100 mA g^{-1} in the voltage range 3.00-0.01 V versus Li^+/Li: (a) Pure NiO. Cu_xNiO with incorporated Cu content of (b) 1 % (c) 3 (d) 5%, respectively.

Figure 10. (a) Discharge and Charge capacity vs. cycle numbers curves at a current density of 100 mAg^{-1} and (b) Rate capability of at different current densities from 100 to 1600 mA g^{-1} in the voltage range 3.00-0.01 V versus Li^+/Li for 60 cycles of Cu_xNiO samples with 0, 1, 3, 5% Cu incorporated.

Figure 11. Discharge and Charge capacity vs. cycle numbers curves of $Cu_{3\%}NiO$ samples calcinated at temperature of 350, 450, 550 °C at a current density of 100 mA g^{-1} in the voltage range 3.00-0.01 V versus Li^+/Li for 100 cycles.

Figure captions

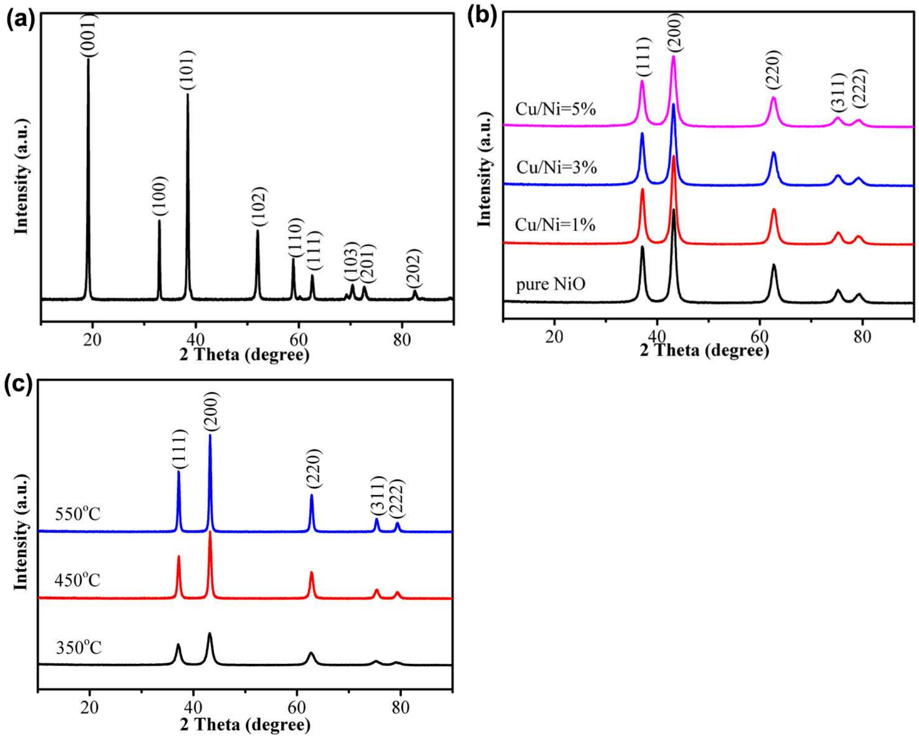

Figure 1. X-ray diffraction (XRD) patterns for (a) $Ni(OH)_2$ precursor, (b) pure NiO and Cu_xNiO with 1, 3, 5% incorporated Cu contents. (c) Comparison of XRD pattern for $Cu_{3\%}NiO$ calcinated at 350, 450, 550°C, respectively.

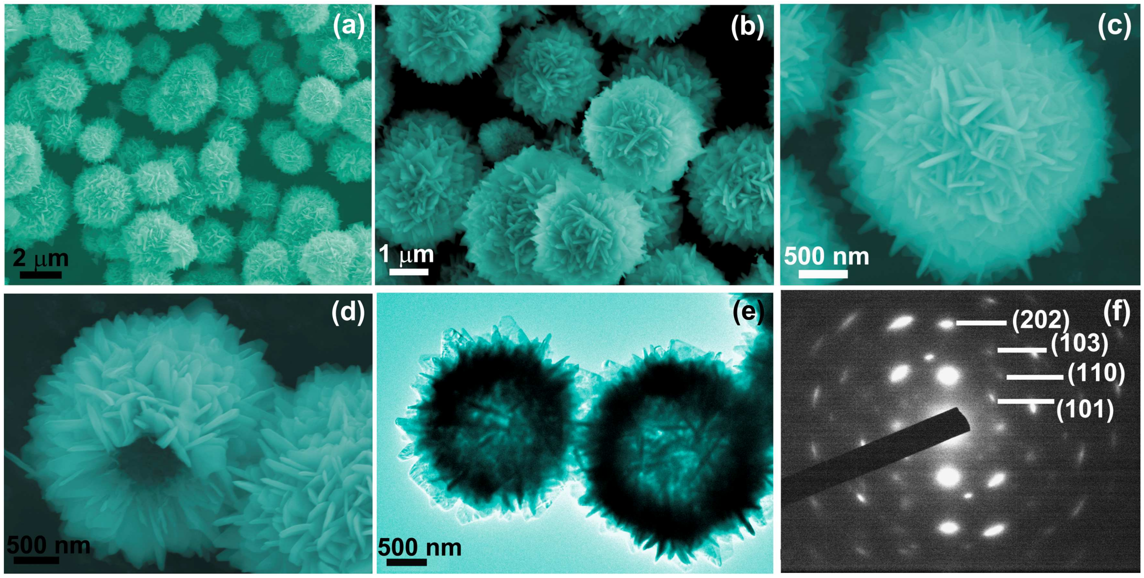

Figure 2 (a-d) Low- and high-magnification FESEM images of 3D hierarchical Cu-doped $Ni(OH)_2$ products spherical architectures. (e) Low magnification TEM image of Cu-doped $Ni(OH)_2$. (f) Electron diffraction pattern suggests a polycrystalline nature for the Cu-doped $Ni(OH)_2$ products. The diffraction rings correspond well to (101), (110), (103), (202) planes of hexagonal Cu-doped $Ni(OH)_2$.

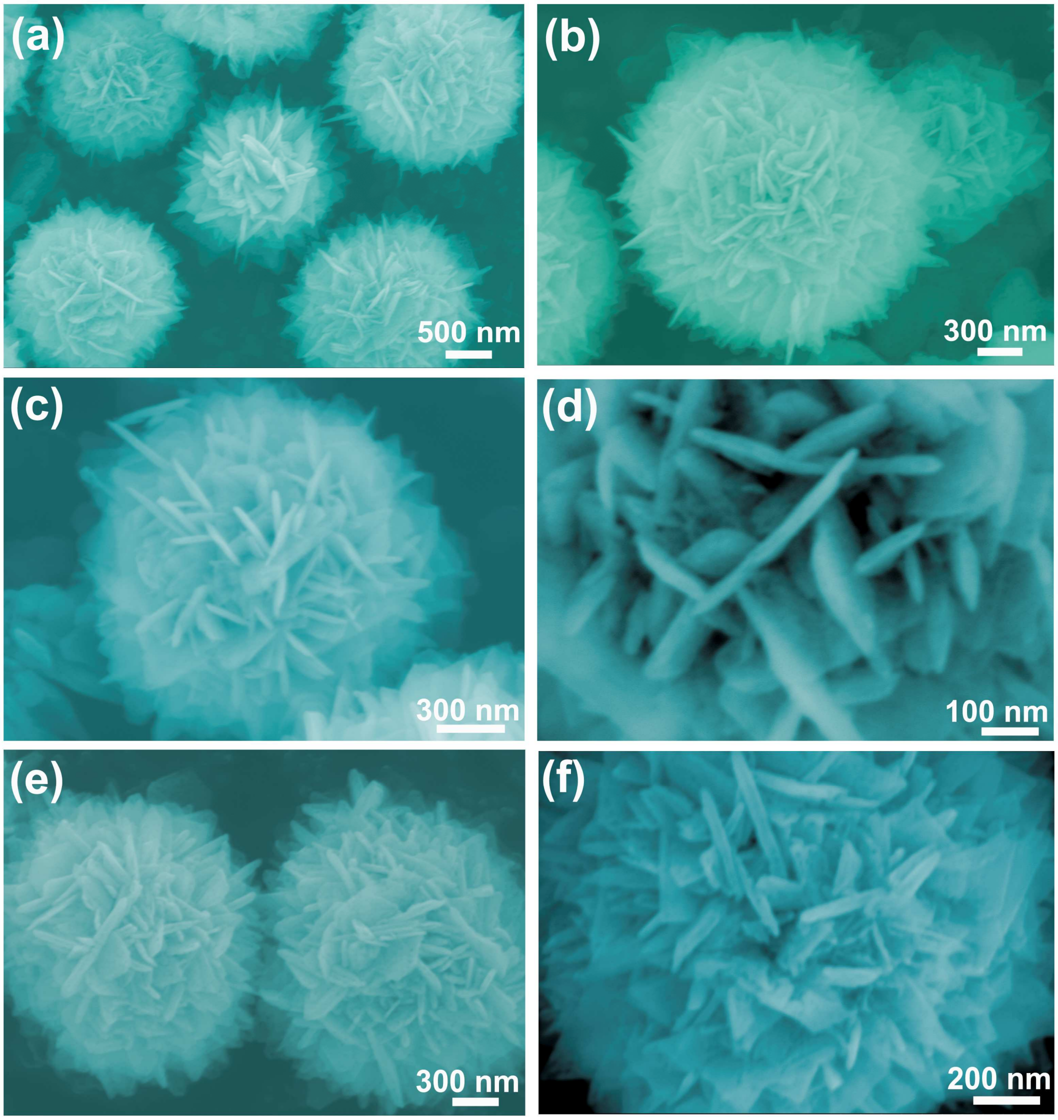

Figure 3 (a-b), (c-d), (e-f) Low- and high-magnification FESEM images of the $Cu_{3\%}NiO$ products prepared at a calcination temperature of 350, 450, 550°C for 2 h, respectively.

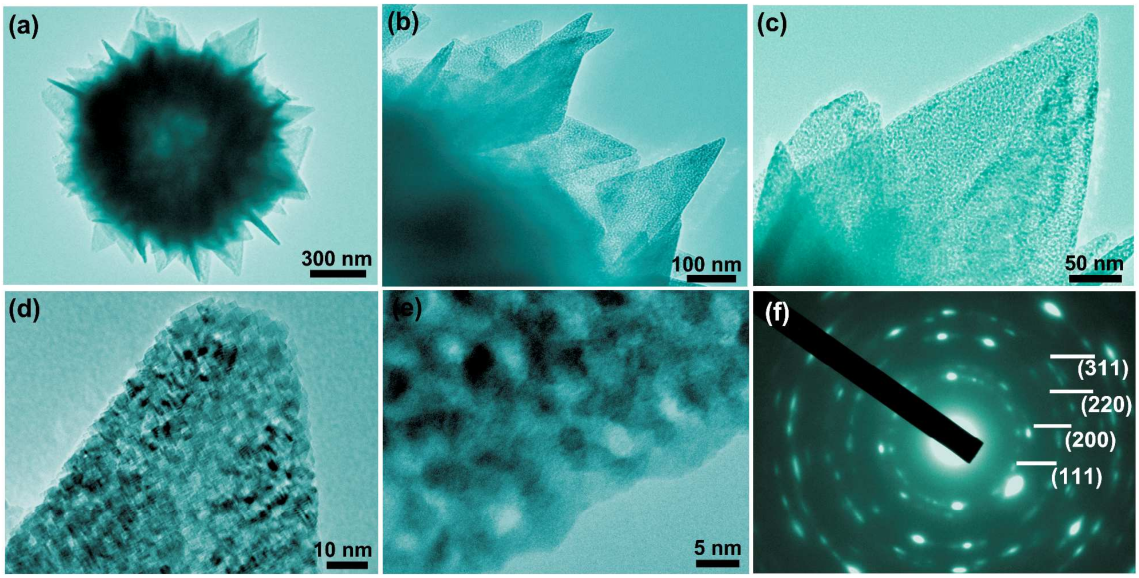

Figure 4 (a) Low magnification TEM image of Cu$_{3\%}$NiO sample thermally calcinated at 350°C. (b) An enlarged TEM image taken from the edge of the 3D hierarchical Cu$_{3\%}$NiO samples in Fig. 4b clearly suggests the 3D hierarchical Cu$_{3\%}$NiO sample is composed of two-dimensional (2D) triangular plates. (c) A magnified TEM image indicates a typical porous structure for Cu$_{3\%}$NiO sample. (d-e) High magnification TEM images indicate and mecropores with average size of 8 nm are homogeneously formed within the Cu$_{3\%}$NiO samples, and Cu$_{3\%}$NiO plates are composed of nanocrystals with an average diameter of 10 nm. (f) Electron diffraction concentric diffraction rings could be assigned to (111), (200), (220), (311) planes of cubic Cu$_{3\%}$NiO.

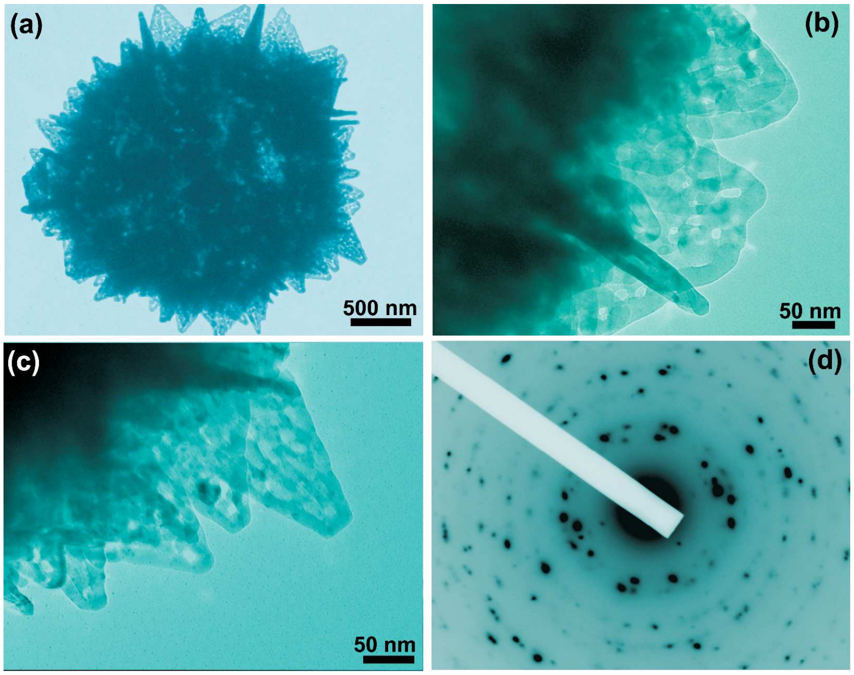

Figure 5 (a) Low magnification TEM image of Cu$_{3\%}$NiO sample thermally calcinated at 550°C. (b-c) Magnified TEM images of the triangular Cu$_{3\%}$NiO plates, clearly showing the porous structures, with an average size of 20-25 nm for the pores in the Cu$_{3\%}$NiO plates. Such larger pores could be owing to the faster elimination of water molecules from Ni(OH)$_2$ precursor at the relatively higher calcination temperature. (d) The diffraction rings could be assigned to the (111), (200), (220), and (311) planes of cubic Cu$_{3\%}$NiO.

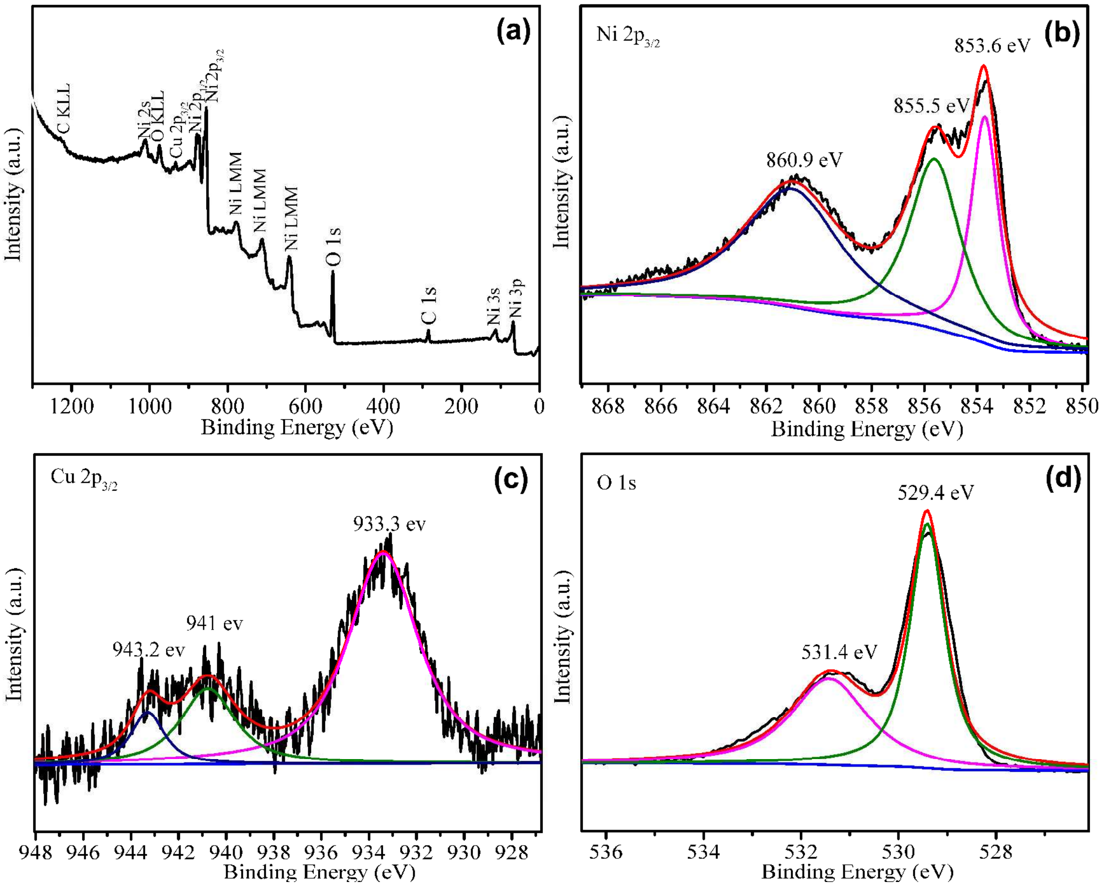

Figure 6 (a) Survey XPS spectrum for the as-prepared $Cu_{3\%}NiO$ sample. (b) XPS spectra of Ni 2 $P_{3/2}$. (c) XPS spectrum of Cu 2 $P_{3/2}$. (d) O 1s XPS spectrum of $Cu_{3\%}NiO$ sample.

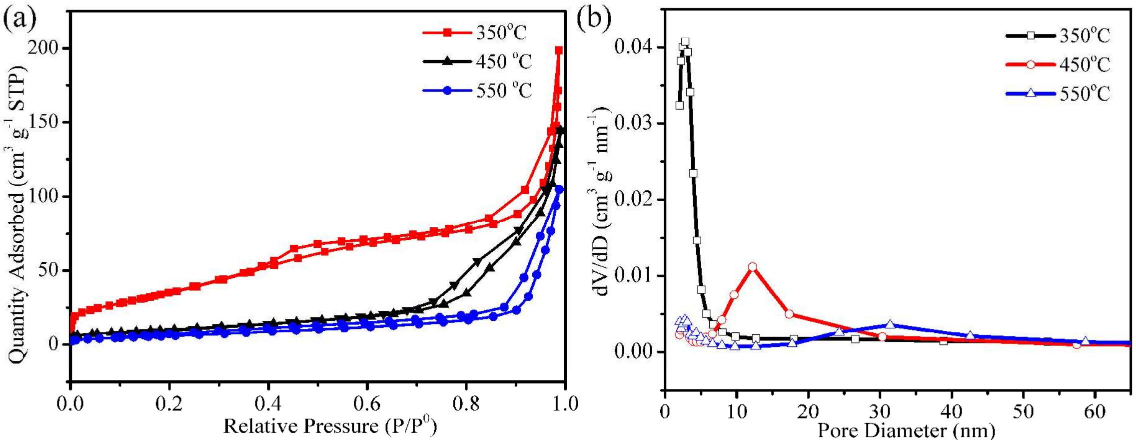

Figure 7 Porous structure analysis of $Cu_{3\%}NiO$ samples calcinated at 350, 450, 550°C, respectively. (a) Nitrogen adsorption/desorption isotherm and (b) pore size distribution.

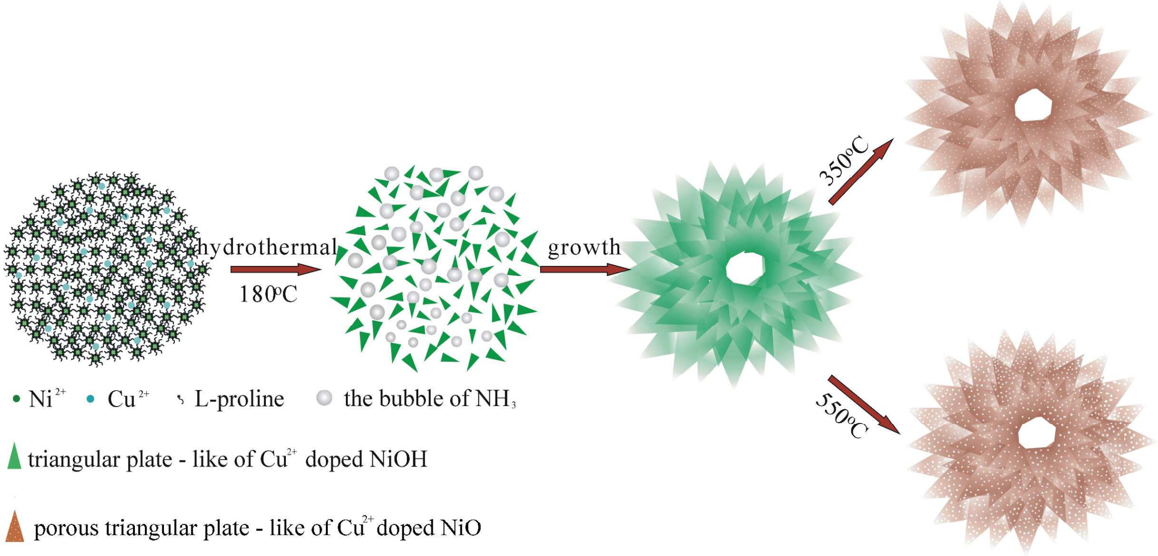

Scheme 1 Schematic illustration for the possible growth of as-synthesized hierarchical hollow mesoporous Cu_xNiO nanostructures.

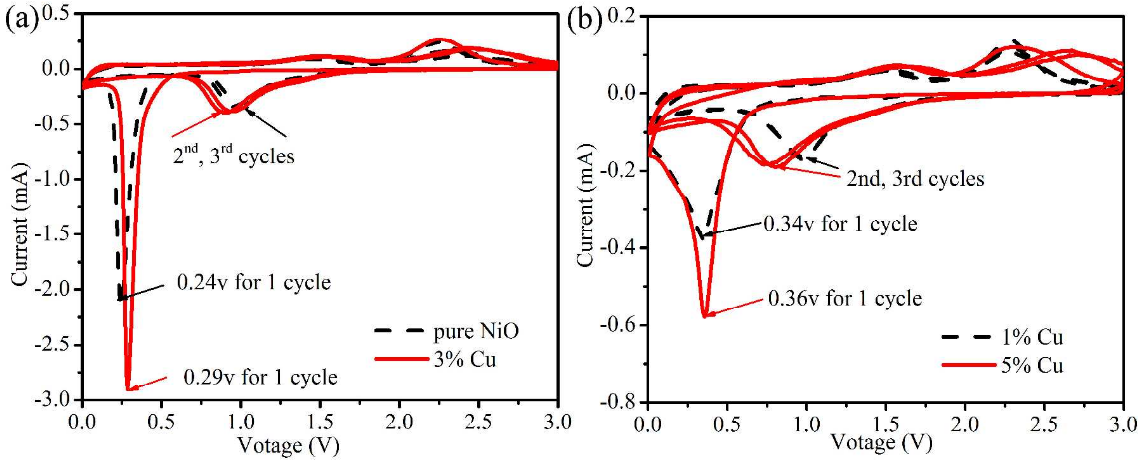

Figure 8 (a, b) CV curves for three cycles at a scan rate of 0.1 mV s^{-1} in the voltage range of 3.00-0.01 V of the pure NiO, Cu_xNiO samples calcinated at 350°C with different Cu incorporated contents of 1, 3, 5%, respectively.

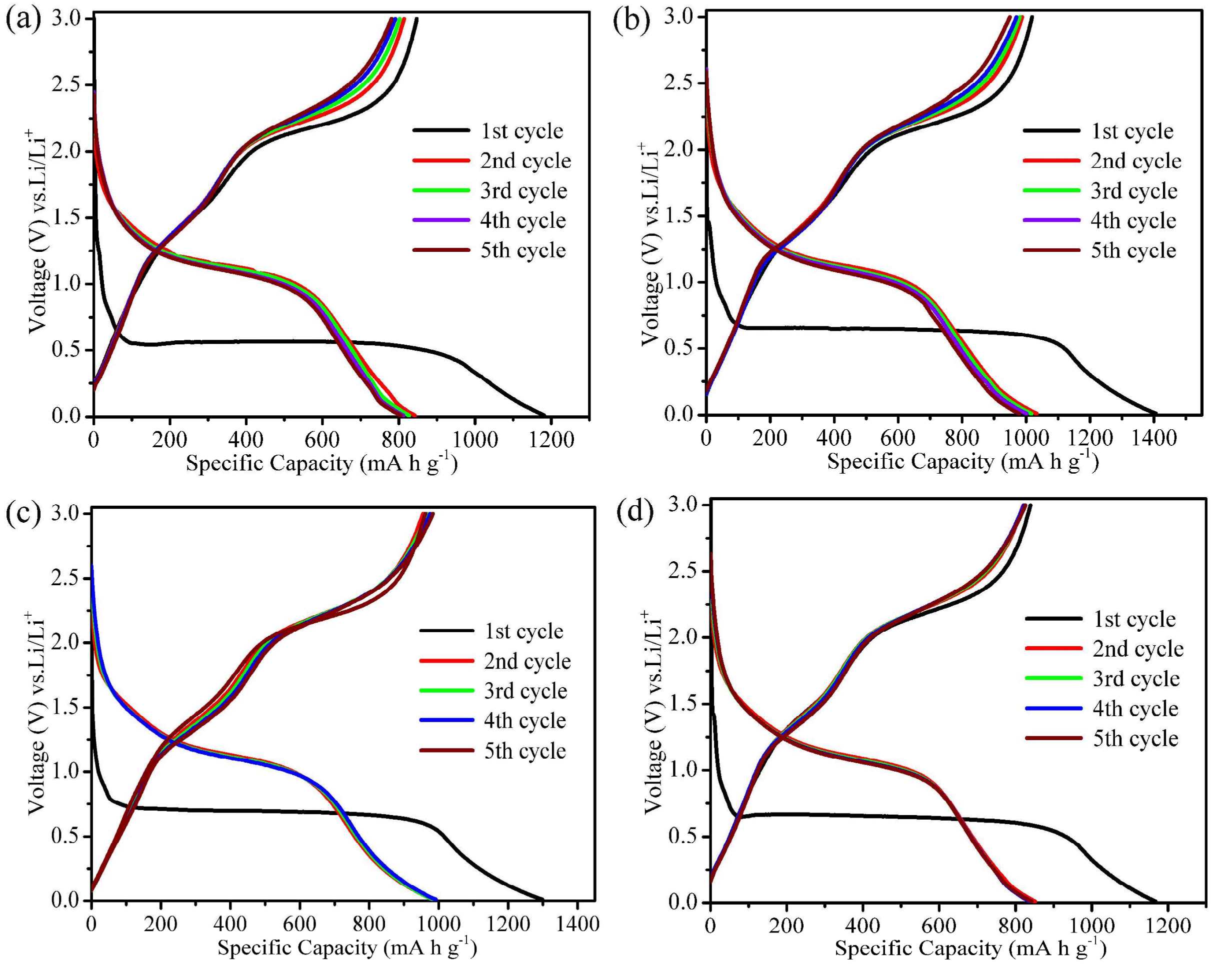

Figure 9. Discharge-charge profiles of electrode at a current density of 100 mA g^{-1} in the voltage range 3.00-0.01 V versus Li$^+$/Li: (a) Pure NiO. Cu$_x$NiO with incorporated Cu content of (b) 1 % (c) 3 (d) 5%, respectively.

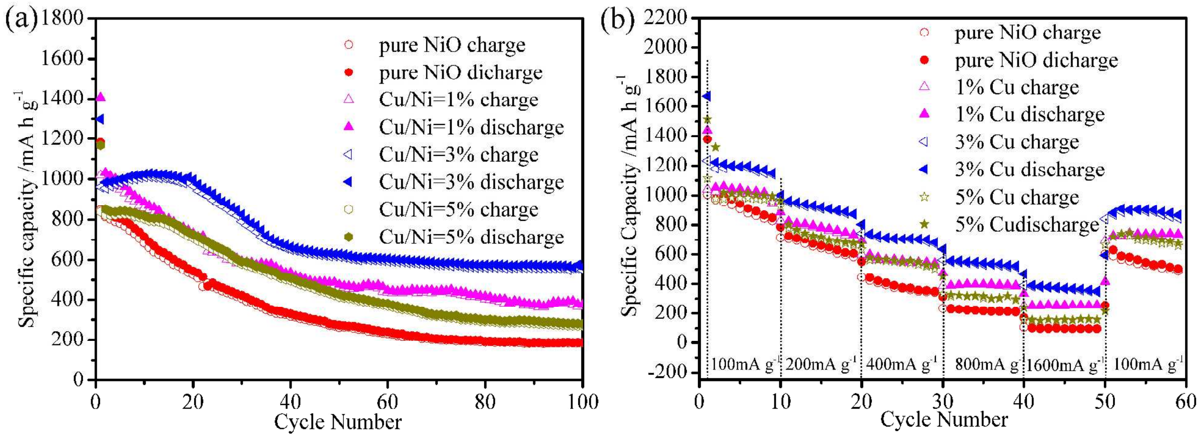

Figure 10. (a) Discharge and Charge capacity vs. cycle numbers curves at a current density of 100 mAg^{-1} and (b) Rate capability of at different current densities from 100 to 1600 mA g^{-1} in the voltage range 3.00-0.01 V versus Li^{+}/Li for 60 cycles of Cu$_x$NiO samples with 0, 1, 3, 5% Cu incorporated.

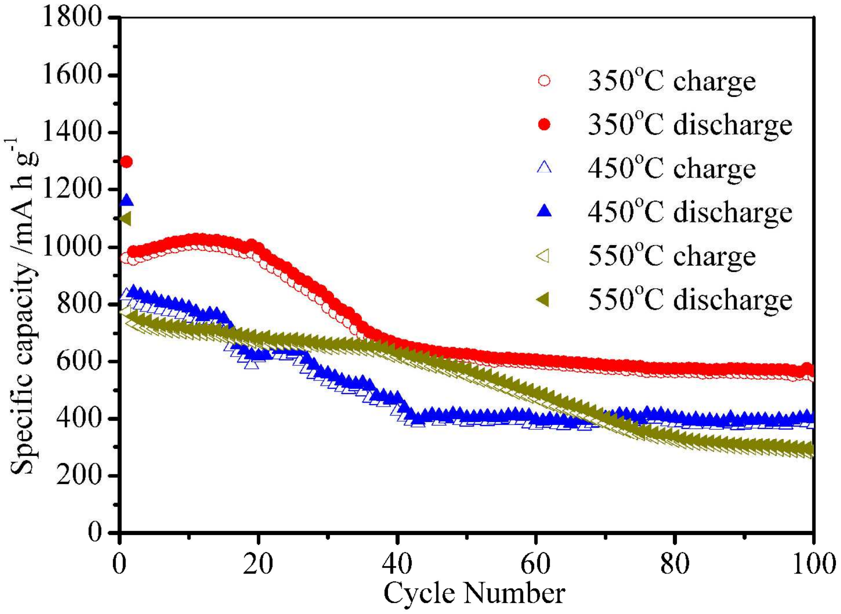

Figure 11. Discharge and Charge capacity vs. cycle numbers curves of Cu$_{3\%}$NiO samples calcinated at temperature of 350, 450, 550 ^{o}C at a current density of 100 mA g^{-1} in the voltage range 3.00-0.01 V versus Li^{+}/Li for 100 cycles.